Novel operating mode of a fluidic oscillator

Chris J. Nicholls
Post-Doctoral Research Assistant
Oxford Thermofluids Institute
Department of Engineering Science
University of Oxford
Oxford, UK
Email: christopher.nicholls@eng.ox.ac.uk

Brian M. T. Tang
Post-Doctoral Research Assistant
Oxford Thermofluids Institute
Department of Engineering Science
University of Oxford
Oxford, UK

James Turner
Post-Doctoral Research Assistant
Oxford Thermofluids Institute
Department of Engineering Science
University of Oxford
Oxford, UK

Marko Bacic
University Research Lecturer
Oxford Thermofluids Institute
Department of Engineering Science
University of Oxford
Oxford, UK
Seconded part-time to OTI from Rolls-Royce plc

ABSTRACT

Fluidic oscillators show promise for use in aerodynamic flow control applications, with many studies reporting oscillation frequencies in the 1–10 kHz range. Spyropoulos [1] introduced a 'sonic' oscillator whose oscillation frequency depends on the inlet flow rate. The purpose of this paper is to demonstrate the existence of a second mode of operation (Mode II) for such an oscillator, with a separate physical mechanism to the traditional, flow rate-dependent mode (Mode I). Mode II is shown to be a back-pressure driven oscillation that is largely independent of flow rate once instigated. This is explained by a stationary wave formed along the outlet paths, and occurs when conditions on the degree of back pressure and the weakening of the Coandă attachment strength

are met. For a fixed device geometry, the conditions reduce to a minimum flow rate threshold, so that the combination of high flow rate and constant oscillation frequency could make Mode II an attractive flow control solution in an industrial context where minimising device size is often critical.

NOMENCLATURE

Miscellaneous

β Sine wave argument scaling parameter
b Inlet nozzle width
c Speed of sound
D Attachment wall setback distance
$D_{[x]}$ Tube internal diameter
$f(x)$ Initial pressure distribution along outlet path
$\bar{f}_{[x]}$ Limiting Mode II frequency for $L_\mathsf{O} = x$ cm
F_s Sampling frequency
$L_{[x]}$ Tube length
$p(t, x)$ Time series pressure measurement at position x
Re Reynolds number
x Distance along outlet path from splitter tip

Subscripts

CP Control port tube
O Outlet tube
O,c Outlet channel from splitter tip to outlet fitting
V Venting tube

Abbreviations

LHS Left hand side
RHS Right hand side
RMS Root mean square
PSD Power spectral density
slpm Standard litres per minute
uRANS Unsteady Reynolds-averaged Navier-Stokes

1 INTRODUCTION

Since their conception at the Harry Diamond Laboratories in 1959, fluidic devices have been the subject of many research studies [2]. Their popularity in a modern research context is a result of their potential to provide a reliable means of actuating fluid flows [3]. Many articles have been written about the application of fluidic devices to problems such as flow separation control [4–7], cavity suppression control [8], tip leakage control [9–11], and thrust vectoring [12]. The present work is motivated by the challenge of controlling fluid flows in aerospace applications, which typically require reliable actuators with significant authority and relatively high bandwidth (on the order of kHz in some cases) [13]. Fluidic actuators have the potential to overcome these challenges, with recent studies making strides into understanding their operation and improving bandwidth and authority limitations [14–16]. Switching time uncertainty is addressed by Nicholls *et al.* [17] through the use of closed-loop control. Since they contain no moving parts, fluidic devices do not suffer from wear and therefore require less maintenance. Moreover, they offer potential reductions in cost and weight over traditional mechanical equivalents. Feedback fluidic oscillators have some kind of feedback mechanism, allowing the device to produce self sustained oscillations when supplied with a pressurised fluid. These typically have a higher continuous switching bandwidth than diverters that are controlled with either an external fluid supply or a separate actuator, e.g. plasma or acoustic [18]. There

are two common designs of feedback oscillators: relaxation fluidic oscillators, introduced by Warren [19], which have two feedback paths and use a portion of the main jet total pressure to switch itself, and 'sonic' oscillators, introduced by Spyropoulos [1], which have one feedback path and use the pressure difference that keeps the jet curved and attached to the wall to drive the oscillation. The widely-used NASA relaxation fluidic oscillator design has dominated flow control studies in the literature, e.g. [20–22]. Strides have been made to control its phase [23] as well as to assess its effectiveness as an actuator in unsteady heat transfer [24, 25]. The design style by Spyropoulos [1] has seen relatively little research interest. However, the relaxation oscillator design is likely to suffer from inherently higher pressure losses because of the nature of the oscillation mechanism — momentum is bled from the main jet into the feedback paths. The sonic oscillator does not siphon off any of the main jet total pressure, therefore allowing a greater maximum potential efficiency.

Early research on the modelling of reattaching jets, the core component of most fluidic devices, began with the work of Bourque & Newman [26] and Sawyer [27], which was applied to model the switching process in a fluidic diverter by Lush [28, 29] and others [30–32]. More recently, modelling work resulted in the prediction of fluidic oscillator operating frequency [33, 34]. However, studies involving fluidic oscillators have typically considered them in isolation. Flow impedances and perturbations at the device outlets could have a significant effect on the oscillation mechanism. Rotating turbomachinery, passing flow structures, or serially-connected pneumatic devices (such as fluidic diverters in multi-staged systems) could disrupt oscillator performance. In this paper, focus is placed on a hitherto unstudied fundamental operating mode of sonic oscillators that is driven by the outlet impedance if conditions on the back pressure and the weakening of jet attachment are met.

Most fluidic devices are governed by the Coandă effect, the tendency of a fluid jet to attach to a nearby surface [35]. When supplied with a pressurised fluid, a jet issues from a nozzle and entrains the surrounding ambient fluid (Fig. 1). The jet surroundings are confined by the attachment walls, which causes the pressure on either side to reduce. Geometrical imperfections or random perturbations result in an asymmetry in the pressure reduction, resulting in the jet attaching to one of the side walls. Upon striking the wall, the angle of the jet and the low pressure between the jet and the wall cause flow to be recirculated into the enclosed region. This stabilises the pressure there and a recirculation bubble is formed.

Spyropoulos [1] proposed a fluidic oscillator design where feedback is provided by a tube connecting the sides of the device to one another (Fig. 2a). When the jet attaches to wall A, the sharp pressure reduction between the jet and the wall creates an expansion wave that travels along the control port tube (to B in Figure 2a). The wave connects the sides of the jet and relieves the pressure difference, causing the jet to switch to wall B, where the process repeats. The jet oscillates between paths A and B. Unlike the more common relaxation fluidic oscillator introduced by Warren [19], Spyropoulos's design does not use any of the main jet momentum to drive the oscillation and so results in a lower device pressure loss coefficient. Spyropoulos [1] demonstrated a linear relationship between the oscillation frequency and the length of the control port tube, L_{CP}. As a result, it was suggested that for a wide range of values of L_{CP} and flow rates, the propagation time of the pressure and expansion waves in the control port tube dominates the oscillation, and the jet switching time is small by comparison. However, in [1] it was found that (a) the oscillation frequency decreased when the diameter of the control port tube, D_{CP}, was reduced, and (b) the oscillation frequency increased with the flow rate at a given value of L_{CP}. Spyropoulos suggested that the jet switching time caused both of these effects.

In this paper, tubes terminated with valves are connected to the outlets of a fluidic oscillator of the type introduced by Spyropoulos [1] to study their effect on the oscillation mechanism. A second mode of operation (Mode II), is found to occur at certain flow conditions, and is identified to have a separate physical mechanism to the traditional mode of device operation characterised by Spyropoulos [1] (Mode I). Once instigated, the insensitivity of the Mode II oscillation frequency to flow rate, as well as its occurrence at high flow rates, could make it an attractive flow control strategy in industrial contexts.

2 EXPERIMENTAL SETUP

The device was designed in a modular fashion and manufactured by polyjet printing. The internal diverter design is shown in Fig. 3a, with dimensions in Fig. 3b. The important features are an attachment wall setback (jet centreline to downstream edge of control port channel) of D =1.3b, where $b = 2$ mm is the inlet nozzle width, and the attachment wall angle is 6°. The aspect ratio is 3, giving a device depth of 6 mm. The splitter is 8b downstream of the nozzle orifice. The Sensortechnics HCXPM010D6 and HCXM350D6 pressure transducers were used for all experiments, with National Instruments NI 9205 ADC and NI cRIO 9035 used for data acquisition. Data were sampled at $F_s = 50$ kHz after the signal was passed through a 25 kHz, 1st order anti-aliasing filter. Total pressure measurements from pitot probes in the outlet channels were used to determine the oscillation frequency. The inlet, outlets, and control ports were bolted to fittings that consisted of a lofted surface from the rectangular cross-section of the main device to the relevant circular size to match the flexible tubing (control port channels & outlets) or pipe fitting (inlet) inner diameter. Each length of outlet tubing was connected to a ball valve in order to control the back pressure. Care was taken to avoid abrupt changes in cross section which would cause an impedance mismatch. The connections are shown in Fig. 4, where D_{CP} and L_{CP} are the inner diameter and length of the tube connecting the control ports, and D_O and L_O are the internal diameter and length of the tubes connecting each outlet to its respective valve. The lengths are the centreline length of each tube. In all cases, $D_O = 8$ mm. The mass flow rate was set by an Omega FMA-2612A mass flow controller, which was fed by a 100 psig laboratory supply.

3 NUMERICAL SETUP

Numerical simulations of the oscillator were conducted using commercial CFD software. Unstructured meshes were generated using Ansys ICEM CFD v19.2. Five prism layers were used on all surfaces to allow boundary layer development to be captured. The cells were strongly clustered in the switch interaction region where the critical flow features are found, and elements expand rapidly in the outlet legs and control port loop. The overall mesh sizes were approximately 3.8 million cells. The computational domain can be seen in Fig. 5 and the mesh refinement in the interaction region is shown in Fig. 6.

The numerical simulations were run using Ansys CFX v19.2, a node-centred, finite volume solver. The SST k-ω turbulence model was used in an unsteady formulation, with a physical timestep of 0.1 ms, with a steady RANS solution used for domain initialisation in each case. The high resolution advection scheme was used with the second order backward Euler transient scheme and first order turbulence numerics [36]. The boundary conditions were chosen to match the experimental setup, with a fixed mass flow rate inlet and computational openings at atmospheric pressure specified at the end of the outlet legs. Density variations were modelled using ideal gas behaviour. Convergence was assessed by monitoring the residual histories within each physical timestep and achieving periodicity of key flow variables (in particular, mass flow rate variation at the outlets). Eight coefficient (inner) loops per physical timestep was found to be adequate to achieve convergence. Grid independence was established by global scaling of the computational mesh size, approximately doubling the number of cells from 3.8 to 7.4 million cells. One configuration was simulated using both meshes, with $L_{CP} = 140$ cm, $D_{CP} = 8$ mm, and $L_O = 40$ cm at 100 slpm, using identical solver setups. The frequencies of oscillation predicted using the two meshes were in agreement to within the limit of temporal resolution available from the physical timestep size, and the time-averaged mass flow rate differed by just 0.25%. With mesh independence demonstrated, the smaller, 3.8 million cell mesh was used for the remainder of the study

4 DEVICE CHARACTERISATION

The oscillating frequency of the device, as measured by pitot probes in the outlet channels (see Fig. 3a), was recorded over a range of mass flow rates and tube lengths. These data are shown in Fig. 7 for $D_{CP} =$

8 mm and Fig. 8 for $D_{\mathsf{CP}} = 5$ mm, with the mass flow rate in standard litres per minute (slpm)[1]. In both cases, $L_{\mathsf{O}} = 40$ mm, with the outlet valves partially closed. For each value of D_{CP}, the data have been split up into two sets to emphasize the change in behaviour for the larger values of L_{CP} (Fig. 7b and 8b), although it should be noted that the scale is the same on all sets of axes. For each value of L_{CP}, the range of flow rates considered was limited at the upper end because the oscillation frequency appeared to have settled.

The general trends observed in Fig. 7a and 8a are consistent with the traditional, Mode I oscillation, as found by Spyropoulos [1] and Tesař *et al.* [37]. Mode II oscillation can be observed in figures 7b and 8b where the oscillation frequency changes abruptly then displays a weak flow rate dependence.

5 NUMERICAL RESULTS

Mode II oscillation was observed in unsteady RANS simulations run at several conditions, summarised in table 1. The two outlet tube length cases considered were 20 and 40 cm. In each of these cases, the control port tubes had dimensions $L_{\mathsf{CP}} = 140$ cm and $D_{\mathsf{CP}} = 8$ mm. Pressure and velocity frames for $L_{\mathsf{O}} = 20$ cm at 100 slpm are shown in Fig. 9, where the oscillation frequency was 481 Hz. These frames show a single half period of the jet switching from the LHS to the RHS of the device (looking in the direction of the flow). It should be noted that only a portion of the outlet tubes are visible in these frames. The values in table 1 for the 40 cm outlet tube case can be compared with the $L_{\mathsf{CP}} = 140$ cm experimental results in Fig. 7b. In the experiment, the oscillation frequencies were around 304 Hz, while the numerically-obtained values ranged between 283 and 286 Hz, a $\sim$6% discrepancy. It seems reasonable that this is within the margin of error between the simulation and the experiments. These frames are discussed in more detail in section 6.

6 OUTLET TUBE EXPERIMENTS

Aside from the weak flow rate dependence of Mode II relative to Mode I, another striking difference is in the spectral content of the signals. Figure 10 illustrates the power spectral density (PSD) of the outlet pitot measurements for $L_{\mathsf{CP}} = 160$ cm, $D_{\mathsf{CP}} = 8$ mm, $L_{\mathsf{O}} = 40$ cm, with 30 slpm for the Mode I case and 180 slpm for Mode II. The notable difference between these spectra is the sharper peak at the dominant frequency for Mode II, where the power is spread across fewer frequency bins than Mode I.

To investigate the Mode II mechanism further, 8 static pressure tappings were installed at 4 cm intervals along a pair of outlet tubes ($L_{\mathsf{O}} = 20$ cm). There were also static tappings on either side of the splitter and over the pitot tubes in the outlet channels (Fig. 3). The control port tube dimensions were $L_{\mathsf{CP}} = 140$ cm and $D_{\mathsf{CP}} = 8$ mm. It is notable that the outlet valves had to be closed off more to instigate Mode II with shorter outlet tubes. These outlet and control port tube dimensions match those in the uRANS data in Fig. 9. The pressures were sampled and compared with the signal on the LHS of the splitter. The oscillation frequency was 478 Hz and the signals were filtered around this frequency with a 2$^{\mathsf{nd}}$ order, 6 Hz-wide Butterworth bandpass filter. The ratio of the RMS of the signals was computed for each comparison, given by

$$\mathsf{RMS}_{\mathsf{ratio}}(x) = \sqrt{\frac{\sum_{k=1}^{k=N} F\left(p(k,x)\right)^2}{\sum_{k=1}^{k=N} F\left(p_{\mathsf{LHS}}(k)\right)^2}}, \tag{1}$$

where $p(k,x)$ is the pressure sample number k at position x, and $F()$ represents the 478 Hz bandpass filter. In addition, the phase difference was calculated, with signals lagging the LHS splitter signal taken as positive phase differences. The RMS ratio and phase lag plots, relative to the LHS splitter pressure, are shown

[1] slpm is a unit that is commonly used in industrial applications and corresponds to litres per minute at standard conditions (0^{o}C, 1 bar).

in Fig. 11a. The magnitude and phase were insensitive to the filter type used. Additionally, the pressure itself along the outlet tubes is plotted in Fig. 11b at several times during the oscillation. Positive x-values refer to distance along the LHS outlet channel and tube from the splitter, whereas negative x-values indicate the position down the RHS outlet ($x = 0$ refers to the splitter tip). The RMS ratio curve resembles the characteristic of a stationary wave with boundary conditions somewhere between a free and fixed end. The phase plot shows that the signals in each outlet tube are approximately in antiphase, which also corresponds to a stationary wave solution. This assertion is supported by the CFD results, which also have the pressures in the outlet tubes in antiphase.

The 1-D wave equation describes the propagation of pressures along the outlet channels and is given by

$$\frac{\partial^2 p}{\partial t^2} = c^2 \frac{\partial^2 p}{\partial x^2}, \tag{2}$$

where c is sonic speed. D'Alembert's solution is given by

$$p(t,x) = \frac{1}{2}\left(f(x+ct) + f(x-ct)\right), \tag{3}$$

when the pressure is initially constant and described by $f(x)$. If $f(x)$ is approximated to be sinusoidal, it is given by

$$f(x) = \sin\left(\frac{\beta\pi x}{L_{\mathrm{O}} + L_{\mathrm{O,c}}}\right), \tag{4}$$

where $L_{\mathrm{O,c}} = 5\,\mathrm{cm}$ is the length of the outlet channel between the splitter and the position where the outlet tube connects to the device, so that $L_{\mathrm{O}} + L_{\mathrm{O,c}}$ is the distance from the splitter to the outlet valve. The value of the parameter β depends on the behaviour of the pressure at the outlet valve, for which there is no measurement available that would allow β to be determined directly. However, its value can be bounded by consideration of the boundary conditions and the available data. When the outlet valve is fully open, the pressure there is fixed to atmospheric pressure so that $f\left(L_{\mathrm{O}} + L_{\mathrm{O,c}}\right) = 0$, which would be satisfied by $\beta = 1$ and corresponds to a node. Since the valve is partially closed, an upper bound, $\beta < 1$, can be applied. The available experimental pressure data in Fig. 11b indicate that the sinusoid should contain the local maxima and minima (the anti-node), which are observed at $x \approx \pm 10\,\mathrm{cm}$. This translates to a lower bound of $\beta > 0.5$. Assuming sonic speed at 291 K, the frequency of the resulting standing wave, $p(t,x)$, matches the experimental data (478 Hz) when $\beta = 0.7$, which satisfies the bounds.

Time series data from the outlet channel pitot probes measured during Mode II operation are shown in Fig. 12. The extremum values of the time series signals in Fig. 12 relative to the mean indicate that the jet is flapping between the outlet channels rather than fully attaching to either side during oscillation. When the jet moves into a given outlet channel, the volume of the outlet tube is filled and the static pressure increases transiently at the valve end. This increase is propagated upstream towards the splitter. At the same time, the jet is moving away from the other side, resulting in an evacuation of the outlet tube on that side, and the equivalent propagation of the dropping pressure towards the splitter. The result of these smoothly-varying pressures is that the pressure difference across the jet increases in the direction that opposes its motion. This can be seen in the CFD simulation frames in Fig. 9 — the pressure plots in the right hand column show how the pressure in a given outlet channel increases as the jet moves towards that side. However, this effect is delayed from the initial movement across because the pressure signals from the outlet valves

take a finite time to propagate to the splitter where they act on the jet. As only a quarter of the length of the outlet tubes is visible, these frames show the velocity and pressure in the region relatively close to the splitter. The jet is in the RHS (bottom) outlet channel by frame 5 as shown by the velocity plot (Fig. 9e), but the pressure plot (Fig. 9f) shows that the pressure in the LHS (top) outlet channel is greater than that in the RHS outlet channel at this time. In fact, the pressure in the RHS outlet channel does not appear to exceed that in the LHS outlet channel until frame 9 (Fig. 9j). The result of this delayed feedback mechanism is an oscillatory response. This is supported by the experimentally-obtained phase data (Fig. 11), which show a 180º phase shift in the pressure signal across the splitter. To illustrate this point, Fig. 13 shows the the RHS and LHS splitter pressure time series and their difference, in the same Mode II experiments that produced Fig. 11a. It is the signal in Fig. 13b that drives the jet in Mode II.

7 MECHANISMS OF JET DETACHMENT

If the control port tube is disconnected and the control ports are covered, the jet attaches to one side and there is no oscillation. This is because the attached side entrainment flow cannot be supplied through the control port, which means that the Coandă effect is at 'full strength' and the pressure difference across the jet is at a maximum for a given flow rate and outlet impedance. If the control ports are connected to atmosphere through an impedance, then the value of the impedance determines the strength of the Coandă effect. A very large impedance, equivalent to covering the control port, maximises the pressure reduction on the attached side as described above. The effect of reducing the impedance is to allow more of the attached side entrainment flow to be drawn through the control port, lowering the pressure deficit on the attached side and reducing the jet curvature. If the impedance is reduced to zero, then the jet does not attach to either side because the entrainment flow can be supplied without a depression. The degree of Coandă effect weakening therefore depends on the impedance connecting each side of the jet to atmosphere. With $L_O = 40$ cm, leaving the control ports open to atmosphere does result in the jet attaching to one side — the impedance of the control port channels alone is sufficient to allow attachment. However, this is only true with these outlet tubes when the outlet valves are fully open. Partial closure of the outlet valves results in the jet detaching fully and splitting equally down each outlet channel (assuming equal outlet impedance).

Closure of the outlet valves results in an increased transverse pressure gradient across the device at the splitter. This pressure difference, which drives the Mode II oscillation, acts to peel the jet off the wall and works against the Coandă effect. This explains why partially closing the outlet valves can cause the attachment to break down when the impedance connecting the control ports to atmosphere is too great to achieve it alone.

8 VENTING TUBES EXPERIMENTS

In order to determine the role of the control port tube in Mode II, experiments were conducted where it was disconnected. Instead, tubes (henceforth referred to as venting tubes) connected each control port to atmosphere. Mode II operation was possible with $L_O = 40$ cm and the outlet valves fully open for a range of lengths of venting tubes. These lengths were $L_V = 0$ (no tubes, control ports open to atmosphere), 4.3, 8, 21, and 61 cm, where it was possible to instigate Mode II at 75 slpm, and which all had an oscillation frequency of 325 Hz. Additionally, it was observed that Mode II could occur with $L_V = 193$ cm venting tubes, although in this case the flow rate had to be increased to 110 slpm and the oscillation frequency was 321 Hz. In all cases, the venting tubes had $D_V = 8$ mm internal diameter, and Mode II was encouraged by applying a temporary back pressure disturbance at one of the outlets (partial covering of one of the outlet valves momentarily).

The fact that Mode II can be instigated with no control port tube connected shows that its effect on the oscillation frequency is of secondary importance. This demonstrates that the Mode II oscillation is not the classical, 'sonic' oscillator mode described by Spyropoulos [1]. For Mode II to be instigated, the Coandă effect must be weakened to some degree by allowing entrainment flow to be supplied through the control

port. A second requirement is to have sufficient back pressure to allow the transverse pressure gradient at the splitter to be strong enough to drive the jet across to the unattached side outlet channel. It can be seen from Figures 7b and 8b that these conditions are met with a given control port tube length once the flow rate reaches a threshold, since the back pressure is determined by the flow rate and the output impedance. This threshold appears to depend on the length of the control port tube and the impedance of the outlet tubes and valves, all of which play a role in satisfying the requirements above.

9 MODE II OSCILLATION FREQUENCY CALCULATIONS

The theoretical upper limit of the Mode II oscillation frequency can be calculated by considering the propagation delay of the pressure signals from the outlet valves to the splitter. This value alone does not incorporate the dynamics of the pressure in the outlet tubes responding to the jet filling and emptying them periodically, nor the dynamics of the jet itself being driven by the splitter pressure difference signal in Fig. 13b. The limiting frequency is given by

$$\bar{f} = \frac{c}{2\left(L_{\mathrm{O}} + L_{\mathrm{O,c}}\right)} \tag{5}$$

where c is the propagation speed and $L_{\mathrm{O,c}} = 5$ cm is the length of the outlet channel between the splitter and the position where the outlet tube connects to the device. The propagation speed is taken as sonic speed at 291 K, which is $c = 342$ m/s, giving a limiting oscillation frequency of $\bar{f}_{40} = 380$ Hz when $L_{\mathrm{O}} = 40$ cm, and $\bar{f}_{20} = 684$ Hz when $L_{\mathrm{O}} = 20$ cm. This value of $\bar{f}_{40}$ is greater than all of those in Figures 7b and 8b; the largest Mode II frequency observed was 323 Hz ($L_{\mathrm{O}} = 40$ cm, $L_{\mathrm{CP}} = 120$ cm, $D_{\mathrm{CP}} = 8$ mm). Similarly, $\bar{f}_{20}$ exceeds the values recorded in table 1. This is expected because the time taken for the jet to fill and empty the outlet channels as well as move across the device has the effect of lowering the observed frequency.

10 CONCLUSIONS

A fluidic oscillator of the type proposed by Spyropoulos [1] with the addition of outlet tubes and valves has been studied. A previously unstudied mode of operation, named Mode II, was identified. Mode II dominated the traditional operating mechanism (Mode I) when the flow rate exceeded a certain threshold, beyond which it showed a relatively weak flow rate-dependence. Measurements of the pressure along the outlet tubes revealed the presence of a standing wave such that the frequency is largely determined by the length of the outlet channels and tubes. The oscillation was possible because of the delay between the jet moving towards a given outlet channel and the resulting back pressure propagating from the outlet to the splitter, which was clearly illustrated by uRANS data. Experiments were conducted where the control port tube was replaced with venting tubes to connect the sides of the jet to atmosphere through an impedance. The Mode II oscillation was possible in these conditions, illustrating that the role of the control port tube is to weaken the Coandă attachment strength. It was also explained how back pressure works to detach the jet from the wall, working in opposition to the Coandă effect, such that the condition on Mode II occurring is a combination of control port tube impedance, outlet impedance, and flow rate. Finally, calculations of the limiting Mode II frequency at a given outlet tube length based on propagation delay alone showed that all experimental and numerical data satisfied this bound.

ACKNOWLEDGEMENTS

The authors gratefully acknowledge the support of this work by Rolls-Royce and the EPSRC program for active control of fluid flows in gas turbines (EP/L015196/1).

REFERENCES

[1] Spyropoulos, C. E., 1964. "A sonic oscillator". In Proceedings of the Fluid Amplification Symposium, Vol. III, pp. 27–51.

[2] Joyce, J. W., 1983. Fluidics: basic components and applications. Tech. Rep. HDL-SR-83-9, Harry Diamond Laboratories.

[3] Cattafesta III, L. N., and Sheplak, M., 2011. "Actuators for active flow control". *Annual Review of Fluid Mechanics,* **43**, pp. 247–272.

[4] Culley, D. E., Bright, M. M., Prahst, P. S., and Strazisar, A. J., 2004. "Active flow separation control of a stator vane using embedded injection in a multistage compressor experiment". *Journal of Turbomachinery,* **126**(1), pp. 24–34.

[5] Staats, M., and Nitsche, W., 2016. "Active control of the corner separation on a highly loaded compressor cascade with periodic nonsteady boundary conditions by means of fluidic actuators". *Journal of Turbomachinery,* **138**(3), p. 031004.

[6] Staats, M., Löffler, S., Ebert, C., Grund, T., and Weiss, J., 2018. "A fluidic device for active flow control: Simulation vs. experiment with emphasis on application". In 2018 Applied Aerodynamics Conference, p. 3336.

[7] Bauer, M., Lohse, J., Haucke, F., and Nitsche, W., 2014. "High-lift performance investigation of a two-element configuration with a two-stage actuator system". *AIAA Journal,* **52**(6), pp. 1307–1313.

[8] Raman, G., and Raghu, S., 2004. "Cavity resonance suppression using miniature fluidic oscillators". *AIAA Journal,* **42**(12), pp. 2608–2612.

[9] Bae, J., Breuer, K. S., and Tan, C. S., 2003. "Active control of tip clearance flow in axial compressors". In ASME Turbo Expo 2003, collocated with the 2003 International Joint Power Generation Conference, American Society of Mechanical Engineers, pp. 531–542.

[10] Auld, A., Hilfer, M., Hogg, S., Ingram, G., and Messenger, A., 2013. "Application of an air-curtain fluidic jet type seal to reduce turbine shroud leakage". In ASME Turbo Expo 2013: Turbine Technical Conference and Exposition, American Society of Mechanical Engineers, pp. V03AT15A005–V03AT15A005.

[11] Tang, B. M., Bacic, M., and Ireland, P. T., 2017. "Effect of active modulation of through-casing coolant injection on turbine efficiency". In ASME Turbo Expo 2017: Turbomachinery Technical Conference and Exposition, American Society of Mechanical Engineers, p. V02AT40A031.

[12] Raman, G., Packiarajan, S., Papadopoulos, G., Weissman, C., and Raghu, S., 2005. "Jet thrust vectoring using a miniature fluidic oscillator". *The Aeronautical Journal (1968),* **109**(1093), p. 129–138.

[13] Jahanmiri, M., 2010. Active flow control: a review. Tech. rep., Chalmers University of Technology.

[14] Mair, M., Chen, L.-W., Turner, J., Bacic, M., and Ireland, P., 2016. "Experimental and numerical analysis of a piezo driven fluidic device for active flow control". In 52nd AIAA/SAE/ASEE Joint Propulsion Conference, p. 4860.

[15] Mair, M., Turner, J., Bacic, M., and Ireland, P., 2017. "Switching dynamics of a fluid diverter valve using ultrasonic excitation for active flow control". In 47th AIAA Fluid Dynamics Conference, p. 4309.

[16] Mair, M., Bacic, M., and Ireland, P., 2018. "On dynamics of acoustically driven bistable fluidic valves". *Journal of Fluids Engineering*, Oct.

[17] Nicholls, C. J., and Bacic, M., 2020. "Closed-loop control of a piezo-fluidic amplifier". *AIAA Journal,* **58**(6), pp. 2414–2427.

[18] Hak, M. G., 2000. *Flow Control*. Cambridge University Press.

[19] Warren, R. W., 1964. Negative feedback oscillator, Nov. 24. US Patent 3,158,166.

[20] Aram, S., and Shan, H., 2019. "Synchronization effect of an array of sweeping jets on a separated flow over a wall-mounted hump". In AIAA Aviation 2019 Forum, p. 3396.

[21] Sundström, E., and Tomac, M. N., 2021. "Aeroacoustic characteristics of a synchronized fluidic oscillator". *Flow, Turbulence and Combustion,* **106**(1), pp. 61–77.

[22] Gokoglu, S., Kuczmarski, M., Culley, D., and Raghu, S., 2009. "Numerical studies of a fluidic diverter for flow control". In 39th AIAA Fluid Dynamics Conference, p. 4012.

[23] Tomac, M. N., and Gregory, J. W., 2019. "Phase-synchronized fluidic oscillator pair". *AIAA Journal,* **57**(2), pp. 670–681.

[24] Hossain, M. A., Prenter, R., Lundgreen, R. K., Ameri, A., Gregory, J. W., and Bons, J. P., 2017.

"Experimental and Numerical Investigation of Sweeping Jet Film Cooling". *Journal of Turbomachinery,* **140**(3), 12. 031009.
[25] Thurman, D., Poinsatte, P., Ameri, A., Culley, D., Raghu, S., and Shyam, V., 2016. "Investigation of Spiral and Sweeping Holes". *Journal of Turbomachinery,* **138**(9), 04. 091007.
[26] Bourque, C., and Newman, B., 1960. "Reattachment of a two-dimensional, incompressible jet to an adjacent flat plate". *The Aeronautical Quarterly,* **11**(3), pp. 201–232.
[27] Sawyer, R., 1960. "The flow due to a two-dimensional jet issuing parallel to a flat plate". *Journal of Fluid Mechanics,* **9**(4), pp. 543–559.
[28] Lush, P., 1967. "Investigation of the switching mechanism in a large scale model of a turbulent reattachment amplifier(switching time of turbulent reattachment fluid amplifier in large scale model and in theory)". In 2nd Cranfield Fluidics Conference, Vol. 3.
[29] Lush, P., 1968. "A theoretical and experimental investigation of the switching mechanism in a wall attachment fluid amplifier". In Proc. IFAC Symposium on Fluidics.
[30] Epstein, M., 1971. "Theoretical investigation of the switching mechanism in a bistable wall attachment fluid amplifier". *Journal of Basic Engineering,* **93**(1), pp. 55–62.
[31] Goto, J., and Drzewiecki, T., 1972. "An analytical model for the response of flueric wall attachment amplifiers". *Harry Diamond Laboratories, HDL-TR-1598*.
[32] Chang, H. W., 1978. "Dynamic analysis of a monostable fluid amplifier". PhD thesis, Oklahoma State University.
[33] Arwatz, G., Fono, I., and Seifert, A., 2008. "Suction and oscillatory blowing actuator modeling and validation". *AIAA Journal,* **46**(5), pp. 1107–1117.
[34] Wang, S., Batikh, A., Baldas, L., Kourta, A., Mazellier, N., Colin, S., and Orieux, S., 2019. "On the modelling of the switching mechanisms of a coanda fluidic oscillator". *Sensors and Actuators A: Physical,* **299**, p. 111618.
[35] Coandă, H., 1936. Device for deflecting a stream of elastic fluid projected into an elastic fluid, Sept. 1. US Patent 2,052,869.
[36] ANSYS INC., 2019. *CFX Solver Theory Guide*.
[37] Tesař, V., Hung, C.-H., and Zimmerman, W. B., 2006. "No-moving-part hybrid-synthetic jet actuator". *Sensors and Actuators A: Physical,* **125**(2), pp. 159–169.

LIST OF TABLES

Flow rate	$L_{\mathrm{O}} = 20\,\mathrm{cm}$			$L_{\mathrm{O}} = 40\,\mathrm{cm}$		
(slpm)	**uRANS (Hz)**	**Exp. (Hz)**	**Error**	**uRANS (Hz)**	**Exp. (Hz)**	**Error**
100	481	No oscillation	-	283	314	$-9.9\,\%$
125	480	498	$-3.6\,\%$	286	319	$-10.3\,\%$

Table 1: Mode II oscillation frequencies in uRANS with $L_{\mathrm{CP}} = 140\,\mathrm{cm}$, $D_{\mathrm{CP}} = 8\,\mathrm{mm}$, for several flow rates and 20 & 40 cm outlet tube lengths.

LIST OF FIGURES

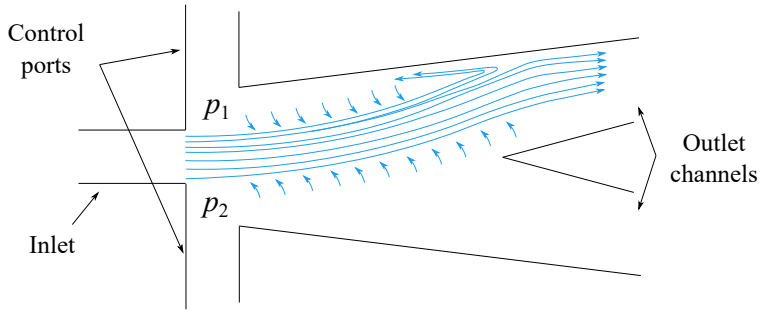

Fig. 1: Fluidic diverter

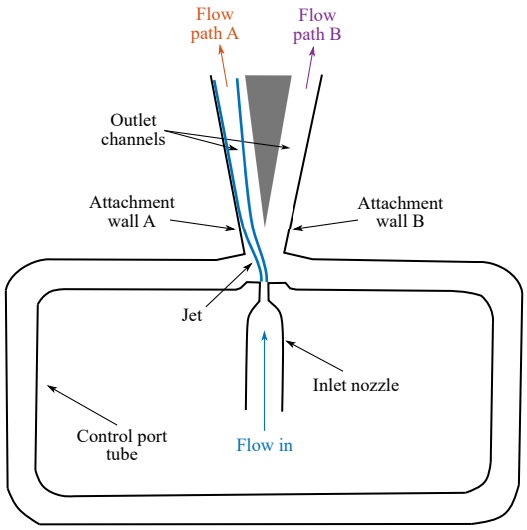

(a) Sonic oscillator, proposed by Spyropoulos [1].

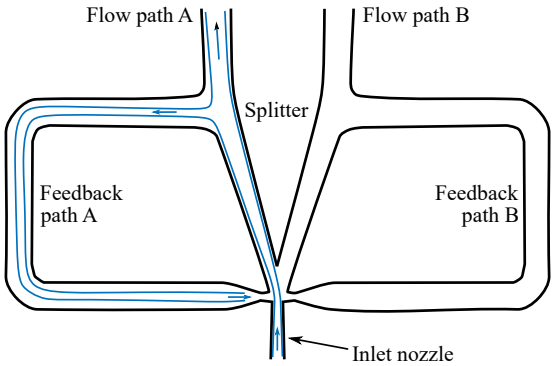

(b) Relaxation fluidic oscillator, proposed by Warren [19].

Fig. 2: Sonic oscillator, 2a, and relaxation fluidic oscillator, 2b.

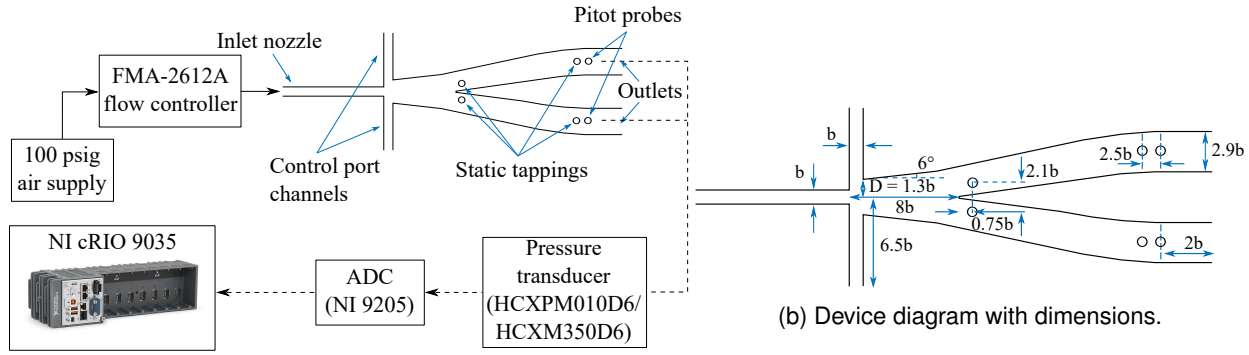

(a) Experimental setup: oscillator internal design and data-collection

(b) Device diagram with dimensions.

Fig. 3: Experimental setup and device dimensions

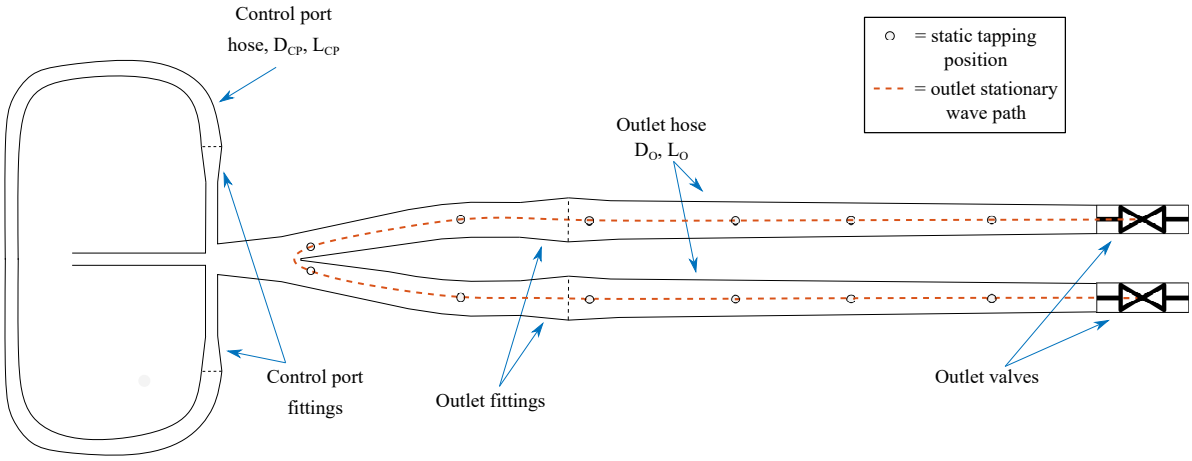

Fig. 4: Experimental setup: Control port and outlet connections

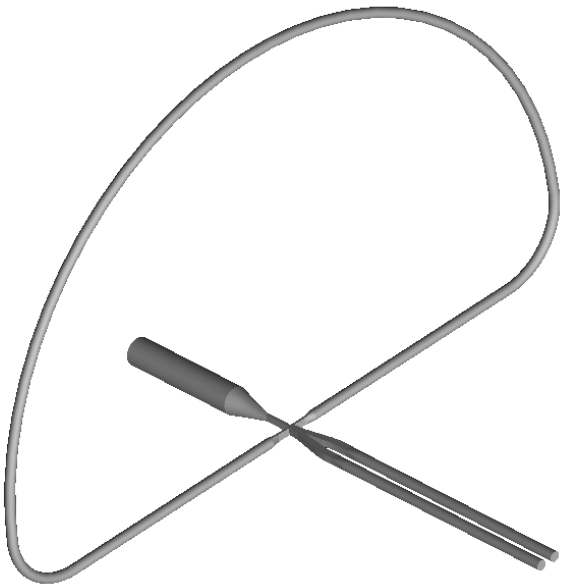

Fig. 5: Numerical setup: computational domain

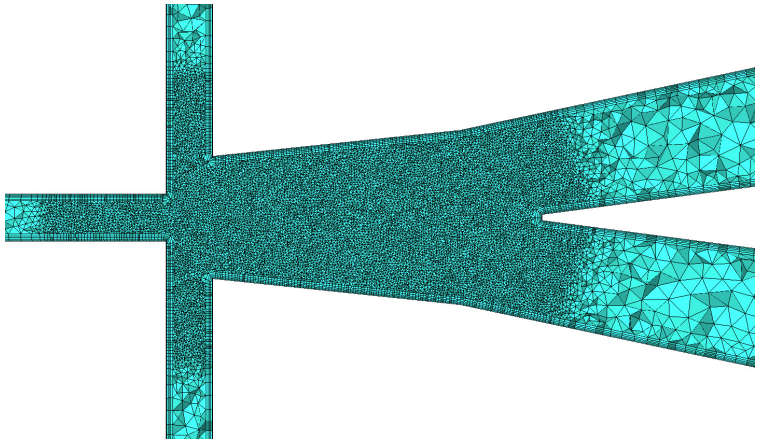

Fig. 6: Numerical setup: mesh in the interaction region

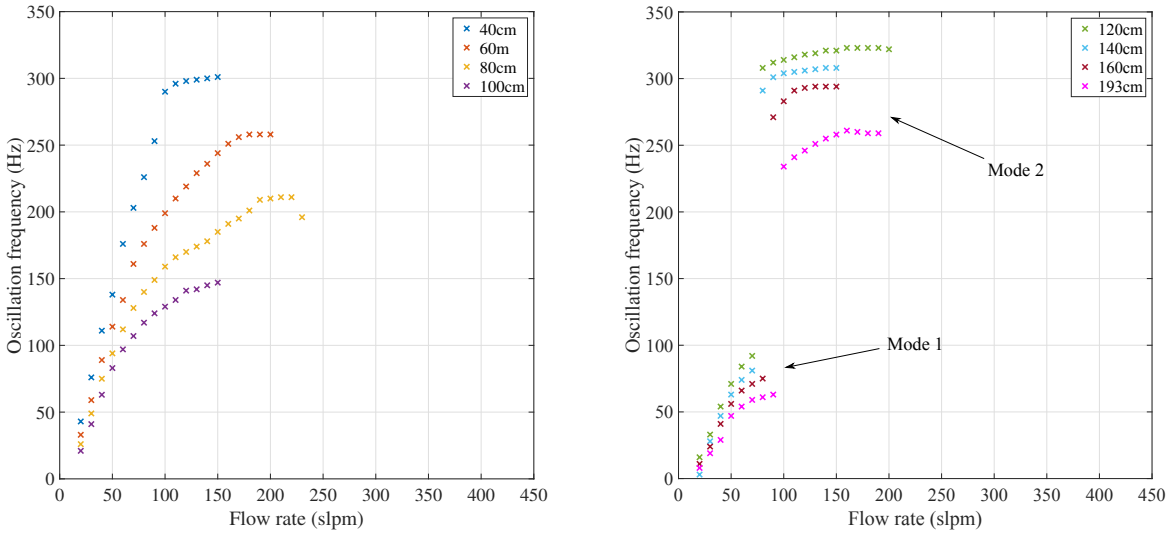

(a) $L_{\mathrm{CP}} = 40$–$100\,\mathrm{cm}$: Mode I only.

(b) $L_{\mathrm{CP}} = 120$–$193\,\mathrm{cm}$: Mode I transitioning to Mode II.

Fig. 7: Experimentally obtained oscillation frequency vs flow rate for several tube lengths at $D_{\mathrm{CP}} = 8\,\mathrm{mm}$: 7a shorter lengths, no jump in frequency; 7b longer lengths, mode change causing jump in dominating frequency.

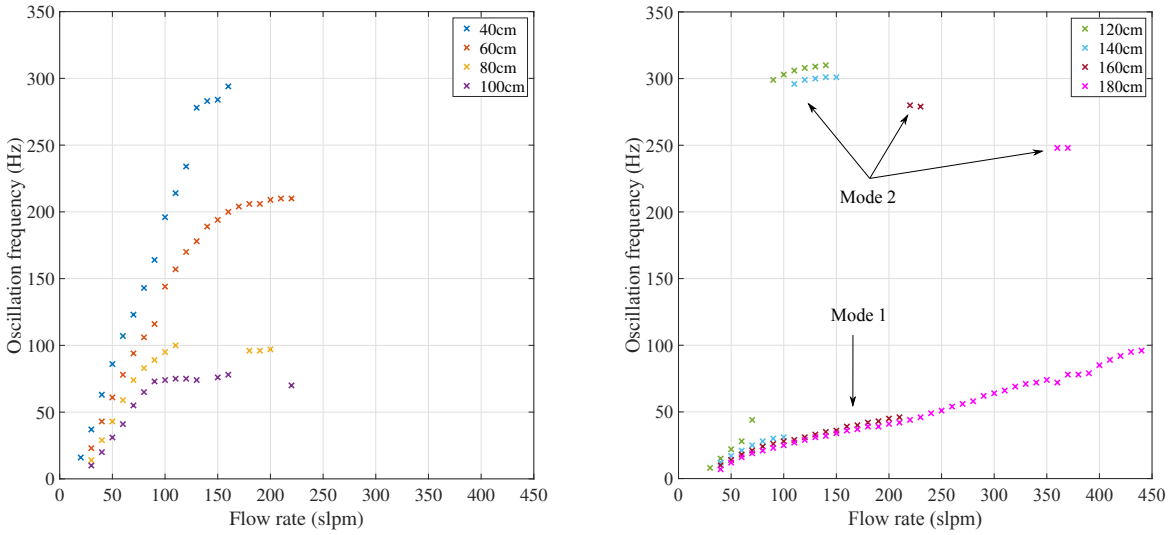

(a) $L_{\mathrm{CP}} = 40$–$100\,\mathrm{cm}$: Mode I only.

(b) $L_{\mathrm{CP}} = 120$–$180\,\mathrm{cm}$: Mode I transitioning to Mode II.

Fig. 8: Experimentally obtained oscillation frequency vs flow rate for several tube lengths at $D_{\mathrm{CP}} = 5\,\mathrm{mm}$: 8a shorter lengths, no jump in frequency; 8b longer lengths, mode change causing jump in dominating frequency.

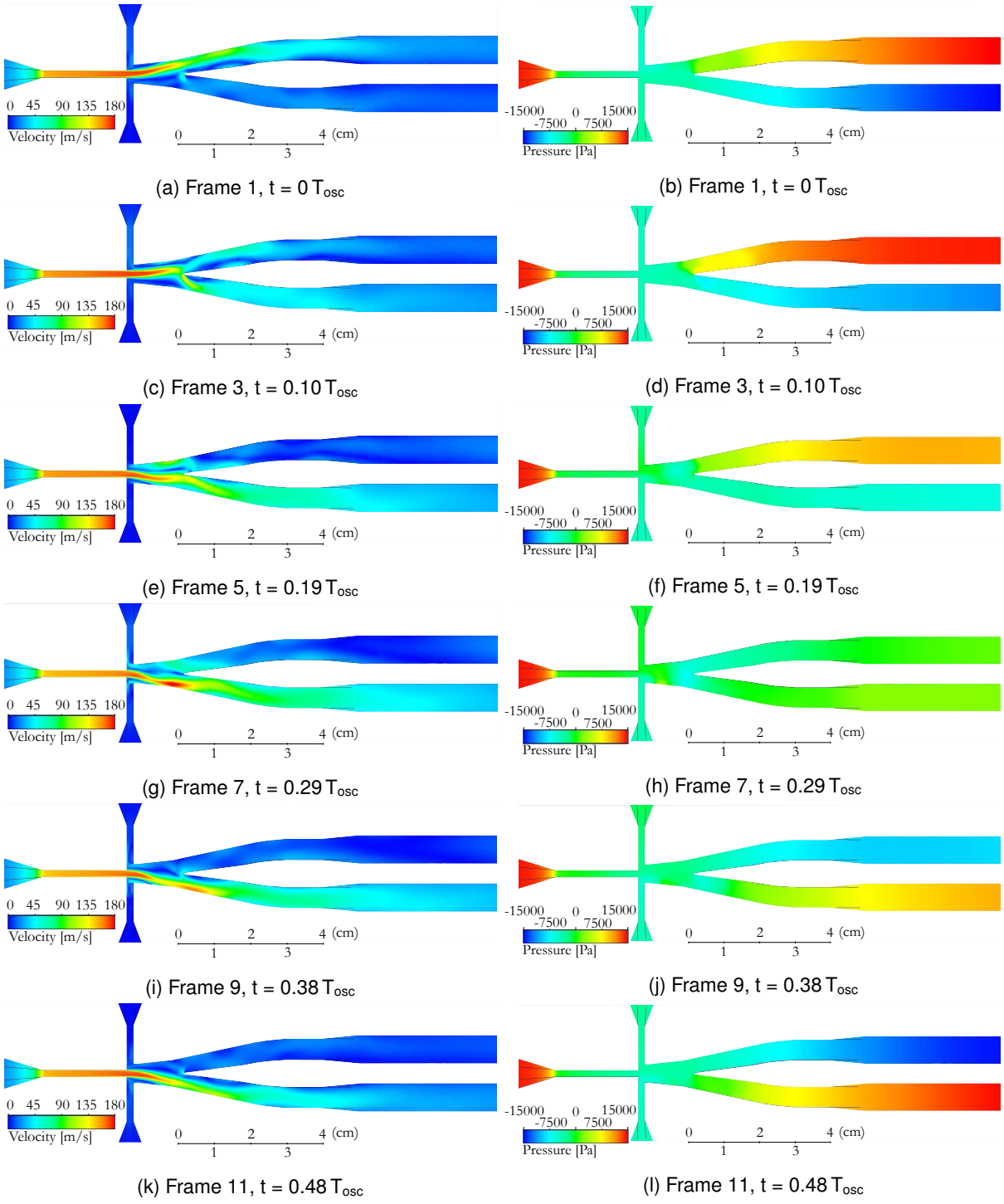

(a) Frame 1, t = 0 T_{osc} (b) Frame 1, t = 0 T_{osc}

(c) Frame 3, t = 0.10 T_{osc} (d) Frame 3, t = 0.10 T_{osc}

(e) Frame 5, t = 0.19 T_{osc} (f) Frame 5, t = 0.19 T_{osc}

(g) Frame 7, t = 0.29 T_{osc} (h) Frame 7, t = 0.29 T_{osc}

(i) Frame 9, t = 0.38 T_{osc} (j) Frame 9, t = 0.38 T_{osc}

(k) Frame 11, t = 0.48 T_{osc} (l) Frame 11, t = 0.48 T_{osc}

Fig. 9: Unsteady RANS data in Mode II, single half period from LHS to RHS: velocity (left) and gauge pressure (right). Parameters: L_{CP} = 140 cm, D_{CP} = 8 mm, 100 slpm, oscillation frequency is 481 Hz. Note that only a portion of the outlet tubes are visible in these frames.

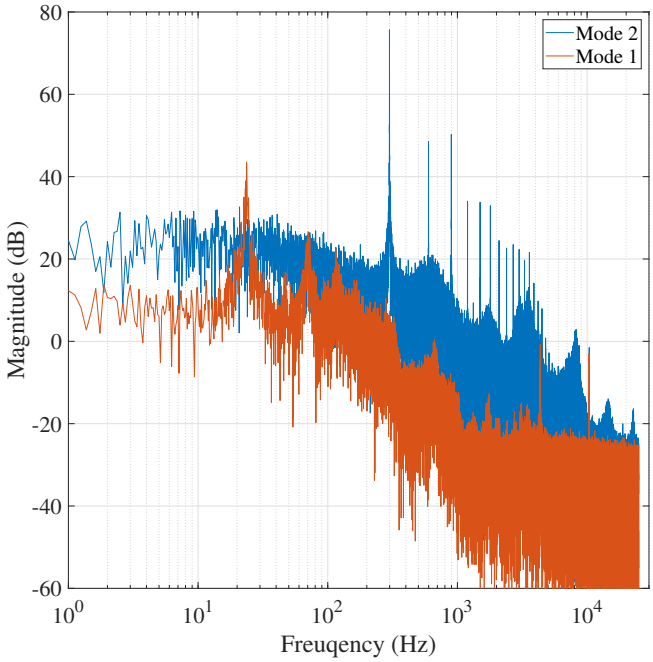

Fig. 10: Spectral comparison: power spectral density of total pressure in outlet channels for 30 (red) and 180 (blue) slpm, with $L_{\mathrm{CP}} = 160$ cm, $D_{\mathrm{CP}} = 8$ mm, $L_{\mathrm{O}} = 40$ cm and $D_{\mathrm{O}} = 8$ mm.

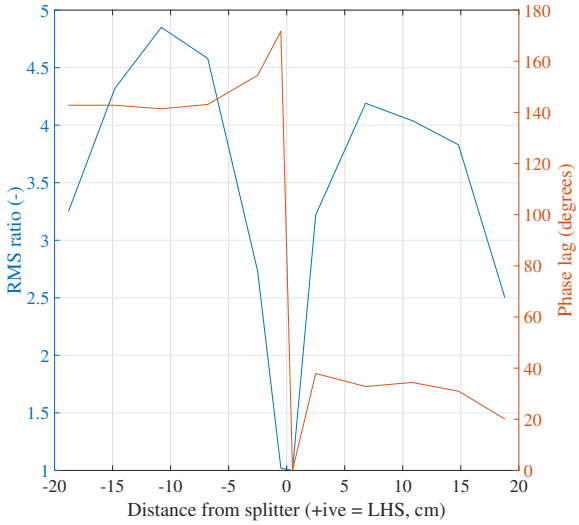

(a) RMS ratio and phase lag of pressure signal at position along outlet tubes relative to signal on LHS of splitter.

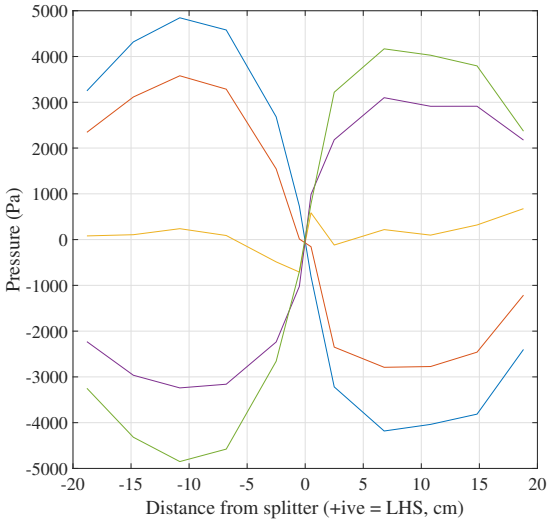

(b) Pressures along outlet tubes at several times during oscillation, demonstrating stationary wave. Phases of -18.8 cm (RHS) signal: 0° (blue), 45° (red), 90° (yellow), 135° (purple), 180° (green).

Fig. 11: Experimentally obtained pressure signals in outlet legs in Mode II: RMS ratio & phase lag (left) and pressure vs position at several times (right). Positive values of x indicate the distance along the LHS outlet channel and tube from the splitter, while negative values refer to the distance along the RHS outlet, with $x = 0$ being the point of the splitter. Parameters: $L_{\mathrm{CP}} = 140\,\mathrm{cm}$, $D_{\mathrm{CP}} = 8\,\mathrm{mm}$, and $L_{\mathrm{O}} = 20\,\mathrm{cm}$, flow rate in Mode II.

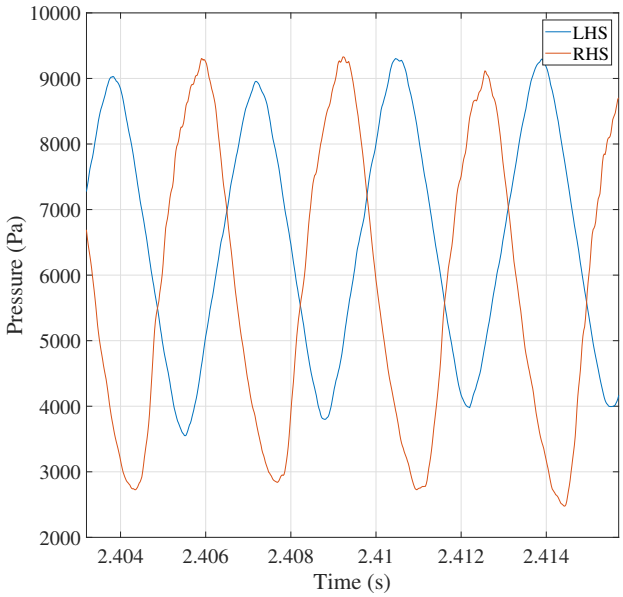

Fig. 12: Experimental total pressure time series data in Mode II in the LHS (blue) and the RHS (red) outlet channels at 180 slpm. Parameters: $L_{\mathsf{CP}} = 160\,\mathrm{cm}$, $D_{\mathsf{CP}} = 8\,\mathrm{mm}$, and $L_{\mathsf{O}} = 40\,\mathrm{cm}$.

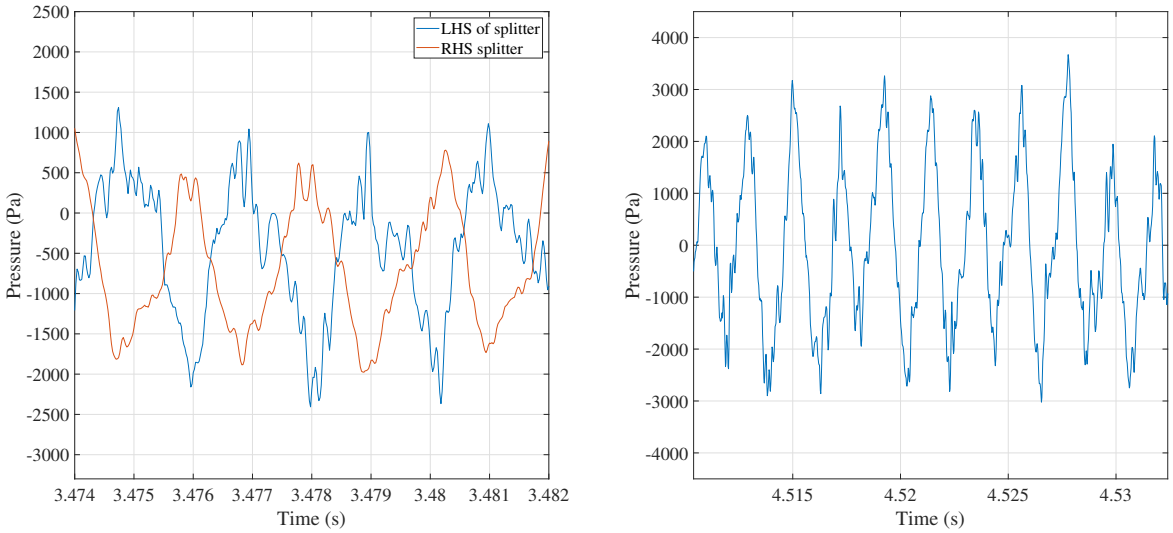

(a) RHS and LHS splitter pressure time series in Mode II.

(b) Difference between RHS and LHS splitter pressure time series in Mode II (RHS − LHS).

Fig. 13: Experimentally obtained time series: LHS and RHS splitter signals (left) and their difference (RHS − LHS, right). Parameters: $L_{\mathrm{CP}} = 140\,\mathrm{cm}$, $D_{\mathrm{CP}} = 8\,\mathrm{mm}$, and $L_{\mathrm{O}} = 20\,\mathrm{cm}$, flow rate in Mode II.